Phys Chem Minerals (2017) 44:735–748
DOI 10.1007/s00269-017-0894-1

ORIGINAL PAPER

Composition–thermal expandability relations and oxidation processes in tourmaline studied by in situ Raman spectroscopy

Anke Watenphul[1] · Thomas Malcherek[1] · Franziska D. H. Wilke[2] · Jochen Schlüter[3] · Boriana Mihailova[1]

Received: 14 March 2017 / Accepted: 25 April 2017 / Published online: 13 May 2017

Abstract The crystal chemistry of tourmaline, $XY_3Z_6(T_6O_{18})(BO_3)_3V_3W$, has a strong influence on the structure and physical properties. Since tourmalines occur in a wide range of geological settings and have large temperature and pressure stability fields, the understanding of the relation between the tourmaline chemistry and thermal expansion allows for better thermodynamic modeling of geological processes. Here, we report dynamic and static thermal expansions as well as mode Grüneisen parameters studied by Raman spectroscopy and single-crystal X-ray diffraction data on several tourmaline species. In addition, oxidation processes in fluor-schorl and Fe^{2+}-bearing elbaite were followed by Raman spectroscopy. Our results emphasize the role of Y-/Z-site occupancy disorder to reduce the local strains and demonstrate that small-size octahedrally coordinated cations perturb the topology of the SiO_4 rings, which in turn seems to enhance the anisotropic thermal-expansion response. In addition, it is shown that the temperature-dependent behavior of the ^{V}OH modes primarily depends on the occupancy of the Y site, whereas that of the ^{W}OH modes depends on the occupancy of the X site. High-temperature Raman experiments in air allowed to follow the oxidation of Fe^{2+} to Fe^{3+} in fluor-schorl by analyzing both the framework and OH-stretching phonon modes. It is further demonstrated that under the same conditions, no oxidation of iron is observed for Fe^{2+}-bearing elbaite, which implies that at high oxygen fugacity, iron is only oxidized in tourmaline species with prevalent divalent cations at the Y site.

Keywords Tourmaline · Raman spectroscopy · Single-crystal X-ray diffraction · Thermal expansion · Mode Grüneisen parameter

Introduction

Tourmalines are borosilicates that crystallize in polar rhombohedral symmetry with space group R3 *m* (e.g., Henry and Dutrow 1996) and have the general chemical formula $XY_3Z_6T_6O_{18}(BO_3)_3V_3W$ (Henry et al. 2011). The crystal structure is characterized by 6-membered TO_4 rings (Fig. 1) with the T site typically occupied by Si and possibly minor contents of Al and/or B. Slightly distorted triangular BO_3 groups are parallel to the trigonal (001) plane. Two octahedrally coordinated cationic positions, a larger Y site and a smaller Z site, link the tetrahedral rings and thus form two types of clusters (Fig. 1): YZZ cluster in which the Y octahedron shares two edges with each Z octahedron and YYY cluster in which each Y octahedron shares an edge with the two adjacent Y octahedra. The octahedral positions display the largest degree of chemical variation. The Z site is dominated by Al^{3+}, Mg^{2+}, Fe^{3+}, but might also contain Fe^{2+}, Cr^{3+}, and V^{3+}. The Y site can host Fe^{2+}, Mg^{2+}, Mn^{2+}, Al^{3+}, Li^{+}, Fe^{3+}, Cr^{3+}, Ti^{4+}, Zn^{2+}, Cu^{2+}, and V^{3+}, and it usually accommodates the trace elements as well (Henry et al. 2011).

✉ Anke Watenphul
anke.watenphul@uni-hamburg.de

✉ Boriana Mihailova
boriana.mihailova@uni-hamburg.de

[1] Fachbereich Geowissenschaften, Universität Hamburg, Grindelallee 48, 20146 Hamburg, Germany

[2] Helmholtz-Zentrum Potsdam – Deutsches GeoForschungsZentrum, Sektion 3.1, Telegrafenberg, 14473 Potsdam, Germany

[3] Centrum für Naturkunde, Mineralogisches Museum, Universität Hamburg, Grindelallee 48, 20146 Hamburg, Germany

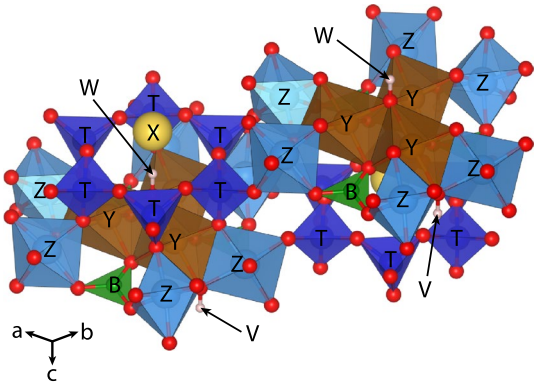

Fig. 1 Crystal structure of tourmaline, space group *R*3 *m*, with X-site cations shown in *yellow*, YO_6 octahedra in *brown*, ZO_6 octahedra in *light blue*, TO_4 tetrahedra in *dark blue*, and BO_3 groups in *green*. V and W sites are occupied by OH groups with hydrogen atoms depicted as *pink balls*. Oxygen atoms are illustrated as *red balls*. The structural data were taken from Ertl et al. (2006) and visualized using the software package VESTA 3 (Momma and Izumi 2011)

The X site, located on the threefold axis of symmetry, is commonly occupied by Na^+, Ca^{2+}, K^+, and vacancies (□). The structure hosts 31 anionic sites of which only O(1) and O(3), named W and V sites, respectively, accommodate ions different from O^{2-}. The V site is shared between one YO_6 and two ZO_6 octahedra, and contains $(OH)^-$ and/or O^{2-}. The W site is shared by the YYY cluster and thus located on the 3-fold axis of symmetry. It can host F^-, $(OH)^-$, and O^{2-} (Henry et al. 2011).

The diversity of possible major, minor, and trace elements that can be incorporated in the tourmaline structure is reflected in the large number of naturally occurring as well as synthetic species that have been identified so far (e.g., Henry et al. 2011; Bosi et al. 2012; Bosi and Skogby 2013; Bosi et al. 2014; Nishio–Hamane et al. 2014; Bosi et al. 2017; Ertl et al. 2016; Hawthorne et al. 2016).

Tourmalines exhibit a macroscopic polarization due to the fact that the apices of all TO_4 tetrahedra in the unit cell point toward the analogous ($-c$) pole (Henry and Dutrow 1996), resulting in an off shift between the center of gravity of anions and that of cations. Macroscopically, this atomic arrangement results in different morphologies of the pyramidal faces on the two poles of the trigonal axis. The chemical composition of tourmalines affects the unit-cell volume. Systematic variations of the unit-cell parameters with element contents at specific crystallographic sites have been observed (e.g., Hawthorne 1996; Bloodaxe et al. 1999; Pieczka 2000; Bosi et al. 2005; Bosi and Lucchesi 2007; Bosi et al. 2010), and they are predominantly related to the different ionic radii of the incorporated elements. Subsequently, the chemical variability also influences the physical properties of tourmalines such as, e.g., pyroelectricy, piezoelectricity, thermal expansion, compression, and heat capacity.

The thermal-expansion behavior of several tourmaline species has been studied over the years using different analytical methods. Donney (1977) used single-crystal X-ray diffraction (SC-XRD) to determine the thermal expansion of an almost Fe^{2+}-free elbaite ($^{Y}Fe^{2+} = 0.09$ apfu; Donney and Barton 1972). Tatli and Pavlovic (1988) studied the thermal expansion of elbaite, schorl, and uvite applying the strain-gauge technique. They observed a distinct influence of the tourmaline chemistry as the linear expansion coefficients α_{ij} decrease from elbaite to schorl to uvite. However, on average, the values derived from strain-gauge experiments for α_{11} are about 73% and for α_{33} about 59% smaller than those reported by Donney (1977). Krishnan et al. (1979) have used interferometry to obtain the thermal-expansion parameters, which are comparable to those of Tatli and Pavlovic (1988). Recently, Pandey and Schreuer (2012) determined the thermal-expansion tensor of five different tourmaline samples with complex chemistry at both the X and Y positions over a large temperature interval using dilatometry. They also found a clear compositional dependence of the thermal expansion on tourmaline chemistry, as the coefficients are lower for Fe^{2+}-rich samples than those for Li-rich tourmalines. Overall, the values are close to those reported by Tatli and Pavlovic (1988) and α_{33} is approximately 2.5 times larger than α_{11} for all studied tourmaline samples.

The piezoelectric response of tourmaline is the strongest along the polar (*c*) axis. Pandey and Schreuer (2012) studied the influence of temperature on the elastic and piezoelectric coefficients by resonant ultrasound spectroscopy. For all samples, they observed that the longitudinal stiffness perpendicular to the *c* axis, c^{E}_{1111}, is larger than that parallel to the *c* axis, c^{E}_{3333}, which indicates that the atomic bonding within the (001) plane is stronger than along the [001] direction. Moreover, the elastic constants show a distinct dependence on Fe^{2+} and Li contents. For Fe-rich, Li-free tourmalines c^{E}_{1111} is higher and c^{E}_{3333} lower than for Fe-free, Li-rich samples. Tourmalines show a typical linear dependence of the piezoelectric and elastic constants with temperature. With the exception of c^{E}_{1123}, all elastic moduli decrease with increasing temperature (Pandey and Schreuer 2012), whereas the temperature derivatives of the longitudinal piezoelectric coefficients d_{111} and d_{333} have opposite signs for most of the samples, thus emphasizing the strong anisotropic response of tourmalines.

Hawkins et al. (1995) studied the compositional influence on the pyroelectric effect in tourmaline. They observed a clear relationship between the pyroelectric responses and the chemistry of tourmalines. Notably, at constant temperature, the pyroelectric coefficient parallel to the *c* axis decreases linearly with increasing FeO content as well as with decreasing Al_2O_3 content. The temperature dependence of the pyroelectric coefficients has

been studied for several tourmaline samples over large temperature ranges from 5 up to 900 K. Above 20 K, the pyroelectric coefficient continuously increases (Hawkins et al. 1995; Zhao et al. 2014) indicating enhancement of the net polarization upon heating, while Gavrilova et al. (1989) showed that for elbaitic tourmalines (exact chemistry unknown), the polarity inverts below 20 K.

So far, the described physical properties and their temperature and compositional dependences have only been studied by techniques sensitive to long-range order. However, the largest chemical variations are typically due to different occupancies of the YZZ and YYY octahedral triplets and also partly to related changes in the anionic V and W sites. Therefore, compositional dependences of the physical properties can also be probed on short-range length scales, e.g., by vibrational spectroscopy.

Raman spectroscopy is a technique well suited for the analysis of chemical variations in complex silicates as it directly probes the local atomic surrounding related with selected phonon modes (Mernagh 1991; Hofmeister and Chopleas 1991; Wang et al. 2001; Leissner et al. 2015; Watenphul et al. 2016a). Recently, we have shown that the content of major and minor elements, including Fe^{3+} and Li, can be determined by the combined analysis of the Raman scattering generated by OH-stretching and framework vibrations (Watenphul et al. 2016a, b; Lensing-Burgdorf et al. 2017). Therefore, temperature-dependent Raman spectroscopy can be regarded as advanced method to study the microscopic influences of chemical variations on the macroscopic physical properties of tourmaline.

The aim of this study is to determine the compositional influence on the phonon thermal expansion of tourmalines by Raman spectroscopy as well as to follow thermally activated oxidation of Fe^{2+} to Fe^{3+} and loss of OH^-. In particular, we will focus on the behavior of the OH-stretching and selected framework vibrational modes and calculated their dynamic thermal expansion coefficients. In addition, the static thermal expansion coefficients were derived via temperature-dependent SC-XRD analysis, and thus, the corresponding Grüneisen parameters were experimentally determined.

Materials and methods

Samples

We examined seven natural single-crystal samples from worldwide localities representative of five different tourmaline species (see Table 1). Polished cuts with an approximate size of 5 × 5 × 2 mm^3 were used for the temperature-dependent Raman spectroscopic measurements, whereas fragments with a maximum linear size of approximately 150 µm were subjected to the temperature-dependent SC-XRD.

Electron microprobe analysis (EMPA)

Chemical analyses of a polished specimen of the samples S60 and S61 were obtained using a Jeol Hyperprobe JXA-8500F with a wavelength-dispersive detector. The energy of the electron beam was 15 keV and the beam current was 20 nA. The following standards were used: fluorite for F; albite for Na; diopside for Mg and Ca; schorl for B, Al, and Fe; orthoclase for Si and K; rutile for Ti, rhodonite for Mn;

Table 1 Chemical compositions of the studied tourmaline samples

#	Species	General formula $XY_3Z_6(T_6O_{18})(BO_3)_3V_3W$						References
		X	Y	Z	T	V	W	
S2	Dravite	$Na_{0.76}Ca_{0.13}\square_{0.12}$	$Mg_{1.91}Al_{0.98}Fe^{2+}_{0.05}Ti_{0.04}$	$Al_{5.2}Mg_{0.8}$	$Si_{6.02}$	$(OH)_3$	$(OH)_{0.76}F_{0.13}O_{0.12}$	Watenphul et al. (2016a)
S60	Dravite	$Na_{0.50}\square_{0.30}Ca_{0.19}$	$Mg_{2.15}Al_{0.66}Ti_{0.04}Cr_{0.01}$	$Al_{5.4}Mg_{0.6}$	Si_6	$(OH)_3$	$(OH)_{0.69}O_{0.29}F_{0.03}$	This study
S61	Fe^{2+}-rich dravite	$Na_{0.70}\square_{0.23}Ca_{0.05}K_{0.01}$	$Al_{1.21}Mg_{1.00}Fe^{2+}_{0.71}Ti_{0.12}$	$Al_{5.3}Mg_{0.7}$	$Si_{5.91}Al_{0.05}B_{0.05}$	$(OH)_3$	$(OH)_{0.77}O_{0.23}$	This study
S8	Fluor-schorl	$Na_{0.76}\square_{0.22}$	$Fe^{2+}_{2.72}Al_{0.24}Mg_{0.02}$	Al_6	$Si_{5.93}Al_{0.07}$	$(OH)_3$	$F_{0.53}(OH)_{0.25}O_{0.22}$	Watenphul et al. (2016a)
S44	Foitite	$\square_{0.61}Na_{0.35}Ca_{0.03}$	$Fe^{2+}_{1.28}Al_{1.03}Mn^{2+}_{0.41}Li_{0.18}Mg_{0.11}$	Al_6	Si_6	$(OH)_3$	$(OH)_{0.93}F_{0.07}$	Watenphul et al. (2016a)
S36	Fluor-buergerite	$Na_{0.79}\square_{0.15}Ca_{0.05}$	$Fe^{3+}_{2.5}Al_{0.30}Fe^{2+}_{0.10}Ti_{0.05}Mg_{0.03}$	Al_6	$Si_{5.93}Al_{0.07}$	O_3	$F_{0.69}(OH)_{0.31}$	Watenphul et al. (2016b)
S19	Fe^{2+}-bearing elbaite	$Na_{0.73}\square_{0.22}Ca_{0.05}$	$Al_{1.25}Li_{1.01}Fe^{2+}_{0.50}Mn^{2+}_{0.22}$	Al_6	Si_6	$(OH)_3$	$F_{0.72}O_{0.17}(OH)_{0.11}$	Watenphul et al. (2016a)

The B site is assumed to be completely occupied by boron, except for S60 and S61 for which boron was analyzed by EMPA and amounts to 3 apfu. Y- and Z-site occupancy disorder was determined by Raman spectroscopy for S2, S60, and S61, and by SC-XRD and Mössbauer spectroscopy for S36. The symbol □ refers to X-site vacancies. The errors in the element contents due to chemical variations amount to 0.05 apfu in maximum

and Cr_2O_3 for Cr. The acquisition times were 10 s for Na, K, and Si; 20 s for F, Ca, Mn, Al, Ti, Mg, Cr, and Fe; and 100 s for B. The acquisition time to collect the background level on both sides of the corresponding peak was half of the peak acquisition time. The program WinTcac (Yavuz et al. 2014) was used to calculate the chemical formulae and also to classify the tourmaline species. The latter was additionally verified by the spreadsheet in the supplement of Henry et al. (2011). About 25–100 spot analyses were carried out for each sample to achieve statistical standard deviations allowing for a compositional precision of about 0.05 apfu for each element in the calculated chemical formulas.

Raman spectroscopy

Raman scattering experiments were conducted with a Horiba Jobin–Yvon S.A.S. T64000 triple-monochromator spectrometer (holographic 1800 grooves/mm gratings) equipped with an Olympus BX41 confocal microscope (Olympus LM Plan FLN 50x objective with a numerical aperture of 0.5) and a Symphony liquid-N_2-cooled charge-coupled device detector. Raman spectra were excited either by the 488.0- or 514.5-nm line of a Coherent 90C Fred Ar^+ laser to ensure minimal photoluminescence background. The spectrometer was calibrated to the T_{2g} mode at 520.5 cm^{-1} of a Si wafer. The achieved spectral resolution was ~2 cm^{-1} and the accuracy in determining the peak positions was ~0.35 cm^{-1}. Polarized Raman spectra were collected in $\bar{y}(zz)y$ scattering geometry (Porto's notation; Porto and Scott 1967), where z was along the crystallographic c axis, while y was parallel to the basal plane.

Measurements were carried out in the temperature range 80–873 K using a Linkam THMS600 heating/cooling stage and a TMS94 temperature controller. For all experiments, the sample chamber was purged with N_2 gas to avoid freezing of atmospheric water on the sample at low temperatures and possible oxidation of Fe^{2+} to Fe^{3+} in Fe-bearing samples at high temperatures. In addition, for samples S8 (fluor-schorl) and S19 (Fe^{2+}-bearing elbaite), Raman spectra at temperatures up to 1150 K were collected in air to allow for the oxidation of iron at high temperatures, using a Linkam TS1200 heating stage and a T95 temperature controller. In all temperature measurements, the sample was kept for 5 min at the desired experimental temperature before the data collection was started to ensure that there was no thermal gradient across the crystal. The acquisition time was chosen to yield a satisfactory signal-to-noise ratio, and thus, most spectra were collected for 20–30 s averaging over minimum 10 accumulations. Note that, first, the Raman scattering from framework vibrations (15–1215 cm^{-1}) was collected and then that from OH-stretching modes (3000–4000 cm^{-1}).

The OriginPro® 9.1 software package was used for data evaluation. The collected spectra were baseline corrected for the continuum luminescence background, and temperature reduced to account for the Bose–Einstein distribution function: $I_{\text{reduced}} = I_{\text{measured}}/(n(\omega,T)+1)$, $n(\omega,T) = 1/(\exp(\hbar\omega/kT)-1)$ with ω being the wavenumber, $\hbar$ the reduced Planck's constant, k the Boltzmann constant, and T the temperature (Kuzmany 2009), and normalized to the acquisition time. Peak positions, full widths at half maximum (FWHMs), and integrated intensities were determined from fits with pseudo-Voigt functions (PV $= (1-q) * \text{Lorentz} + q * \text{Gauss}$, q is the weight coefficient). The criterion for the maximum number of fitted peaks was $\Delta I < I/2$ with I and ΔI being the calculated magnitude and uncertainty of each peak intensity.

Single-crystal X-ray diffraction

Lattice parameters as a function of temperature in the range between room temperature and 550 K have been measured using a Nonius KappaCCD single-crystal diffractometer with graphite monochromated Mo Kα radiation. Single-crystal fragments of tourmaline samples were mounted on quartz glass capillaries using silicone adhesive. In situ heating was performed using a stream of heated air. The temperature was calibrated against the melting points of benzoic acid, 4-methoxybenzoic acid, and caffeine. Lattice parameter refinement based on the position of profile-fitted diffraction maxima has been conducted using the Eval15 suite of programs (Schreurs et al. 2010).

Results and discussion

T-dependent behavior of phonon modes

An exemplary temperature evolution of tourmaline Raman spectra in the range of the framework and OH-stretching vibrations is shown in Fig. 2a and b, respectively, for sample S61 (Fe^{2+}-bearing dravite). As expected, peaks are sharp at low temperatures and broaden upon heating due to the trivial temperature dependence of the phonon damping processes (Kuzmany 2009). Consequently, some peaks start to overlap and become unresolved at elevated temperatures. This can be seen best for the Raman signals between 600 and 715 cm^{-1} originating from SiO_4-ring modes (Fig. 2a). The sharpening of the ^{W}OH-stretching peaks at low temperatures allows to distinguish between the peaks arising from $^{Y}Mg^{Y}Mg^{Y}Mg$-^{X}Na and $^{Y}Mg^{Y}Mg^{Y}Mg$-^{X}Ca species in dravite (sample S2). At room temperature, only one peak near 3770 cm^{-1} attributed to $^{Y}Mg^{Y}Mg^{Y}Mg$-^{X}(Na + Ca) is observed (Watenphul et al. 2016a), whilst at 100 K, two peaks at 3774 and 3784 cm^{-1} are clearly resolved. The

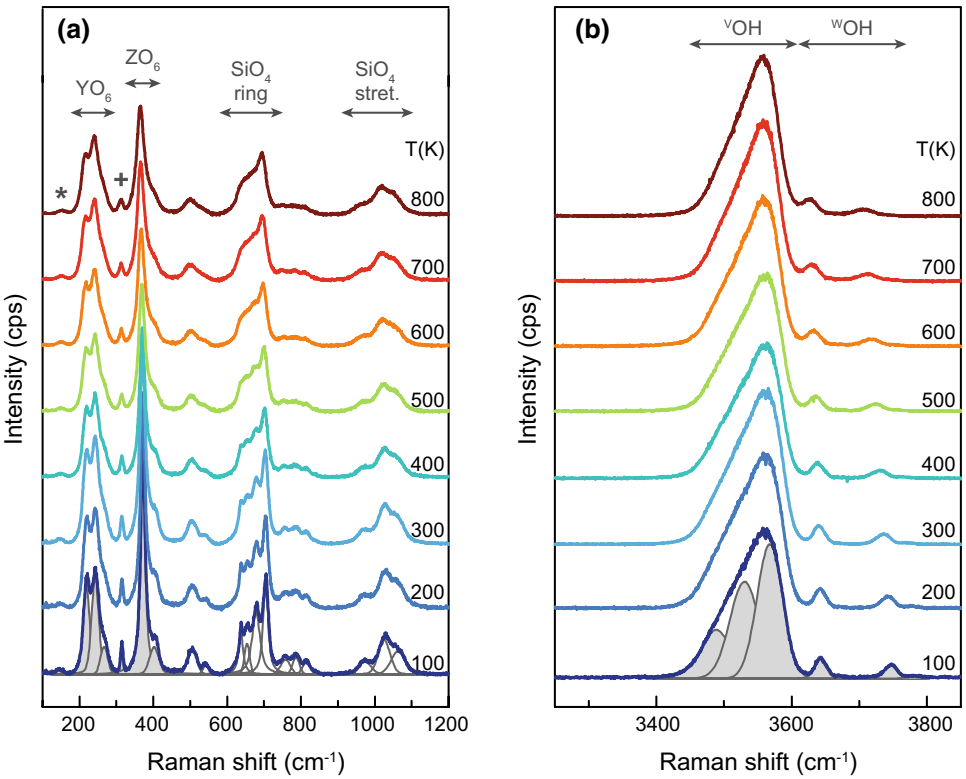

Fig. 2 Polarized $\bar{y}(zz)y$ Raman spectra of Fe^{2+}-bearing dravite (S61) in the spectral region of the **a** framework and **b** OH-stretching vibrations at temperatures from 100 to 800 K. Spectra are vertically offset for clarity. Important ranges of vibrations or vibrational groups are indicated by *arrows*. *Addition symbol* refers to the vibrational mode predominately associated with the linkage of YO_6 and ZO_6 octahedra; *Asterisk* marks the lowest energy mode (see text). Pseudo-Voigt functions used for peak fitting are indicated in *gray*, and functions with shaded areas refer to modes whose positions are analyzed in detail

lower wavenumber peak is assigned to $^{Y}Mg^{Y}Mg^{Y}Mg$-^{X}Na, while the higher wavenumber peak to $^{Y}Mg^{Y}Mg^{Y}Mg$-^{X}Ca, because the higher charged X-site cation has a stronger repulsive effect on adjacent H^+ and consequently a stronger confining effect on the corresponding O–H bond stretching (Gonzalez-Carreño et al. 1988; Watenphul et al. 2016a).

The temperature-dependent behavior of selected framework and OH-stretching vibrational modes is demonstrated for sample S61 (Fe^{2+}-bearing dravite) in Fig. 3a and b. Most of the framework phonon modes show the expected shift toward lower wavenumbers with increasing temperature, due to the increase in the interatomic distances and the consequent decrease in the interatomic force constants. Only the lowest energy mode * (Fig. 3a) exhibits a non-trivial increase in wavenumber upon heating. All Raman-active modes in tourmaline are also infrared-active, i.e., they carry polarity and hence may be influenced by the net polarization, which increases with temperature (Hawkins et al. 1995). Since usually the lowest energy Raman modes comprise vibrations of the heaviest cations against the anionic configurations, one can assume that the dipole moment of * couples with the net polarization of the tourmaline crystal and thus overcomes the typical effect of thermal expansion observed for the other framework vibrations.

With increasing temperature, all ^{W}OH modes shift toward lower frequencies (Fig. 3b), which correlates with the expected primary weakening of the O(1)–H(1) bond strength due to the increase of the O–H bond lengths. Likewise, the most intense ^{V}OH mode, which corresponds to the stoichiometric YZZ–YZZ–YZZ species, shifts toward lower wavenumbers even though the wavenumber change is much smaller over the whole temperature range as compared to the ^{W}OH modes. However, the two lower wavenumber ^{V}OH modes both display shifts toward higher wavenumbers with increasing temperature, suggesting a temperature-induced strengthening of the H bonding, which overcomes the primary effect of enlargement of O–H bond lengths. These modes are related to overcharged YZZ–YZZ–YZZ species, which, in turn, are spatially associated with X-site vacancies (Watenphul et al. 2016a). Therefore, an enhancement of H bonding at elevated temperatures in tourmalines is favored by the absence of X-site cations. Indeed, among the tourmaline samples studied here, anomalous temperature-induced hardening of the ^{V}OH-stretching modes corresponding to overcharged YZZ–YZZ–YZZ configurations is not observed only for S2 (dravite) and S36 (fluor-buergerite), which contain the lowest amounts of vacant X sites (see Table 1).

Composition-thermal expansion relations

In generally, the anharmonicity in the crystal potential due to phonon–phonon interactions causes the interatomic distances to enlarge with increasing temperature,

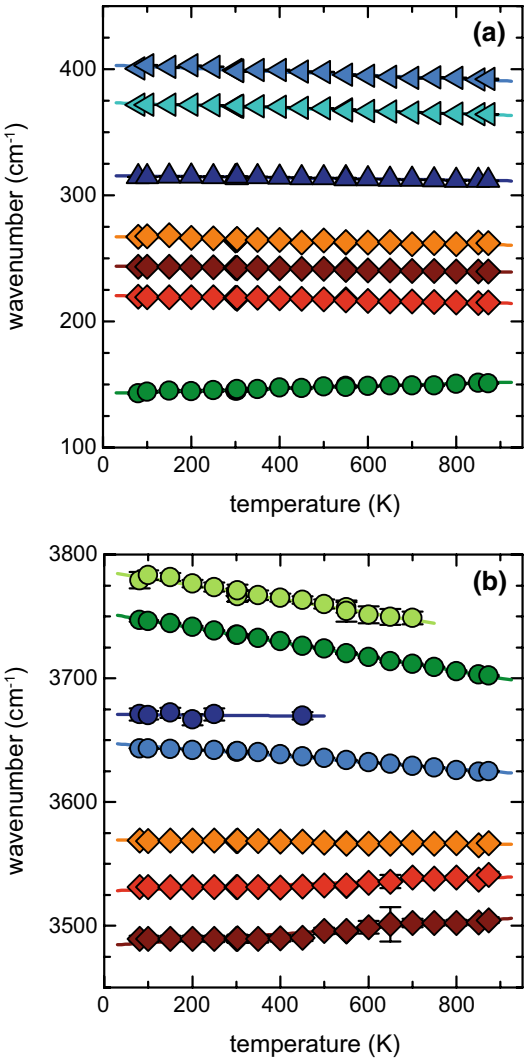

Fig. 3 Positions of selected **a** framework and **b** OH-stretching vibrations of Fe^{2+}-bearing dravite (S61) at temperatures between 80 and 873 K. Vibrational modes belonging to one of the major ranges (see Fig. 2) are depicted by the same symbol. If not visible, errors are within the symbol size. Linear fits to the data points are given by *solid lines*

resulting in thermal expansion of the crystals. Since all phonons in the studied tourmaline samples exhibit a linear temperature dependence $\omega(T) = \omega_0 + (d\omega/dT)T$, one can calculate the phonon thermal expandability $\alpha_\omega = (d\omega/dT)/\omega_0$ from the linear fit of $\omega(T)$ for each phonon. This dynamic parameter corresponds to the static volume thermal expansion $\alpha_V = (dV/dT)/V_0$, and hence, the ratio α_ω/α_V can be used to calculate the isotropic Grüneisen parameter $\gamma_V = -\frac{\delta\omega}{\omega_0}/\frac{\delta V}{V_0}$. However, strictly speaking, the static thermal expansion is a tensor $\alpha_{ij} = \varepsilon_{ij}/\Delta T$ representing the strain ε_{ij} accumulated for a temperature change ΔT. Therefore, the Grüneisen parameter is also a tensor, and it can be calculated as $\gamma_{ij} = -\frac{1}{N}\frac{\alpha_\omega}{\alpha_{ij}} = -\frac{1}{N}\left(\frac{1}{\omega_0}\frac{d\omega}{dT}\right)/\alpha_{ij}$, where N is normalization factor equal to the number of non-zero components of a second-rank matter tensor in a given crystal class; for tourmaline $N = 3$. Furthermore, for uniaxial crystals as tourmalines, there are two independent thermal-expansion coefficients α_{11} and α_{33} and consequently two anisotropic Grüneisen parameters γ_{11} and γ_{33}. Thus, we have used the phonon thermal expandabilities α_ω as well as the anisotropic and isotropic Grüneisen parameters γ_{11}, γ_{33} and γ_V, to study the thermal behavior of tourmalines in dependence of the composition.

Figure 4a shows the phonon thermal expandability of the ^{V}OH-stretching modes as a function of the mean ionic radius $\langle r_{YZZ-YZZ-YZZ}\rangle$ of the YZZ–YZZ–YZZ octahedral triplets that primarily affect the strength of the ^{V}OH bonds. $\langle r_{YZZ-YZZ-YZZ}\rangle$ was calculated for the three major ^{V}OH-stretching modes related to $3^{Y}R^{Z}Al^{Z}Al$, $2^{Y}R^{Z}Al^{Z}Al$-$^{Y}Al^{Z}Al^{Z}Al$, and $^{Y}R^{Z}Al^{Z}Al$-$2^{Y}Al^{Z}Al^{Z}Al$ octahedral configurations with R being the dominant Y-site cation of the respective tourmaline species, e.g., Mg in dravite or Fe^{2+} in schorl. The ionic radii of the respective elements occupying the Y and Z sites in tourmaline were taken from Bosi and Lucchesi (2007). All ^{V}OH-vibrational modes show a clear dependence of the phonon thermal expandability on the chemical composition. The linear fits indicate that the thermal expandability of the mode related to $3^{Y}R^{Z}Al^{Z}Al$, which is the dominant ^{V}OH mode in many tourmaline species (Watenphul et al. 2016a), is least dependent on chemistry, whereas the dependence of the thermal expandability of the ^{V}OH modes at the lowest energies related to $^{Y}R^{Z}Al^{Z}Al$-$2^{Y}Al^{Z}Al^{Z}Al$ has the strongest dependence on the chemical composition (Fig. 4a). This emphasizes the role of ^{Y}Al for the overall thermal behavior of tourmalines.

The phonon thermal expandability of the ^{W}OH modes as a function of the tourmaline chemistry represented by the mean ionic radius $\langle r_{YYY}\rangle$ of the YYY octahedral triplet is shown in Fig. 4b. Interestingly, we do not observe major changes or trends for the same YYY octahedral occupancy in different tourmaline species. For example, all $^{Y}R^{Y}Al^{Y}Al$-$^{X}\square$ modes plot in a narrow regime, no matter whether ^{Y}R is Fe^{2+} in the case of fluor-schorl and foitite, Mg in the case of dravite, or Li and Al in the case of elbaite. This independence of the dynamic thermal expandability of the ^{W}OH modes on tourmaline chemistry is most likely related to the fact that the W site is much stronger influenced by the occupancy of the X site than by the chemistry of the YYY octahedra and temperature. As described above, this strong influence of the X-site occupancy is related with the repulsive interaction of the H^+ cation with the positively charged cation occupying the X site and thus effectively creating a confined

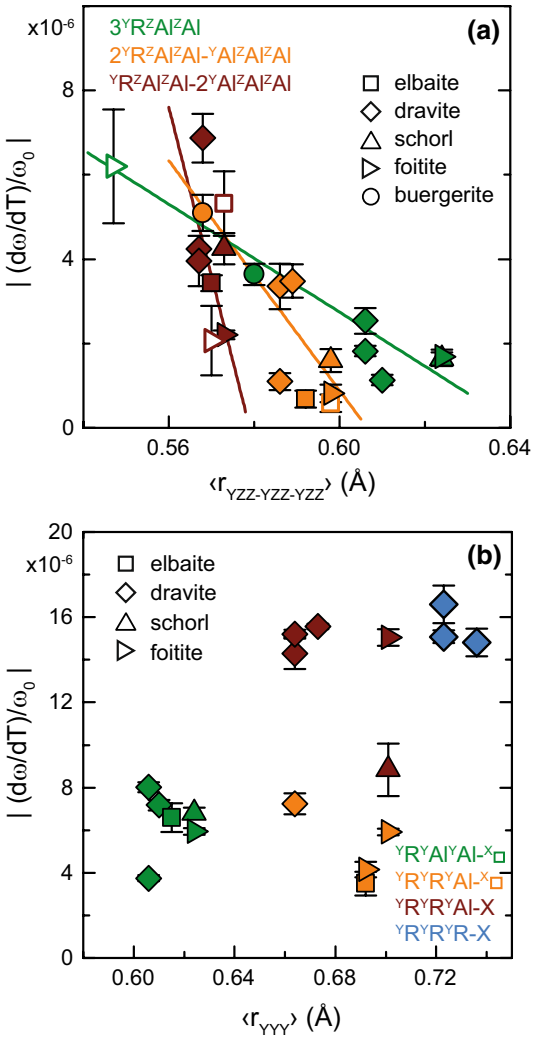

Fig. 4 Phonon thermal expandabilities of **a** ^{V}OH-stretching and **b** ^{W}OH-stretching vibrations in dependence of tourmaline chemistry expressed by the mean ionic radii of octahedral surrounding of the V and W sites, YZZ–YZZ–YZZ and YYY, respectively; R refers to the non-aluminum cations; ω_0 is the peak position of the respective mode at 0 K calculated from linear fits to data points in the range 80–873 K. *Symbol shape* corresponds to the tourmaline species; *symbol color* refers to the chemically distinct octahedral clusters related to the particular OH-stretching mode (see Watenphul et al. 2016a for details on the peak assignment). *Open symbols* in **a** correspond to OH stretching assigned to YZZ–YZZ–YZZ with R being an additional minor element. *Solid lines* in **a** depict linear fits to the data points of each vibrational mode

space of motion for the O–H bond stretching (Gonzalez-Carreño et al. 1988; Leissner et al. 2015; Watenphul et al. 2016a). In tourmaline, this leads to two separate wavenumber regions of the ^{W}OH modes: ~3710–3820 cm^{-1} for ^{W}OH modes related to occupied X sites and ~3615–3685 cm^{-1} for modes associated with vacant X sites (Watenphul et al. 2016a). These two regions can be nicely observed in Fig. 2b. The ^{W}OH modes show a significant broadening and shifting toward lower wavenumbers with increasing temperature. However, the overall spectral shape does not change. An indication for the change of the thermal expansion behavior with the X-site chemistry can be inferred from the data of one dravite and the foitite sample. Figure 4b shows that the thermal expandability of the ^{W}OH-stretching mode related to ^{Y}R^{Y}R^{Y}Al-X species is about twice as large as that corresponding to ^{Y}R^{Y}R^{Y}Al- ^{X}□ species.

The thermal expandabilities of the framework phonon modes exhibit trends with the chemistry, depending on the type of atomic vibrations. Figure 5a shows the thermal expandability of the YO_6 vibrational modes with respect to $\langle r_{YYY} \rangle$. For fluor-buergerite, elbaite, and foitite, only the expandability of the strongest YO_6 mode ω_2 near ~240 cm^{-1} was considered, while for dravite and fluor-schorl, which exhibit two strong peaks in the spectral range ~220–230 cm^{-1}, the expandability of the lower wavenumber mode ω_1 was also taken into account. Overall, the averaged YO_6 expandability does not show a distinct trend with the chemistry at the Y site. However, the difference in phonon expandabilities $|\alpha_{\omega_1} - \alpha_{\omega_2}|$ for dravite (r = 0.66 Å), Fe^{2+}-bearing dravite (r = 0.67 Å), and fluor-schorl (r = 0.75 Å) clearly increases with the incorporation of Fe^{2+} at the Y site. This implies that the structure of dravite experiences the minimum strain, which can be most likely attributed to the occupancy disorder of Mg over the Y and Z site (Hawthorne 1996; Bosi et al. 2010). As Fe^{2+} shows a little affinity to this type of disorder (Bosi et al. 2015a, b), the strain of the crystal structure of these Fe^{2+}-containing samples is increased, as manifested by the larger difference in the thermal expandabilities of YO_6 phonon modes.

The phonon thermal expandability of the YO_6–ZO_6 linkage (marked with "+" in Fig. 2a) as well as that of the dominant ZO_6 vibrational mode near 370 cm^{-1} show a slight decrease with increasing mean ionic radius $\langle r_{YZZ-YZZ-YZZ} \rangle$ (Fig. 5b). Only the data points for elbaite (r = 0.59 Å) and foitite (r = 0.60 Å) deviate from this linear trend. Most probably, this is related to the larger amounts of ^{Y}Al in these tourmaline species. In contrast, we observe a clear trend of the thermal expandability of the highest wavenumber SiO_4-ring breathing mode near 695 cm^{-1} with the chemistry of the YZZ–YZZ–YZZ cluster (Fig. 5c). The thermal expandability for this mode initially increases with the mean ionic radius $\langle r_{YZZ-YZZ-YZZ} \rangle$, and then for a certain threshold value, it reaches saturation. This indicates that the occupancy of the two octahedrally coordinated cationic positions affects the SiO_4-ring topology (mutual orientation of TO_4) to adopt the local strain due to the incorporation of larger size cations.

In addition to studying the phonon thermal expandabilities by Raman spectroscopy, we have evaluated the

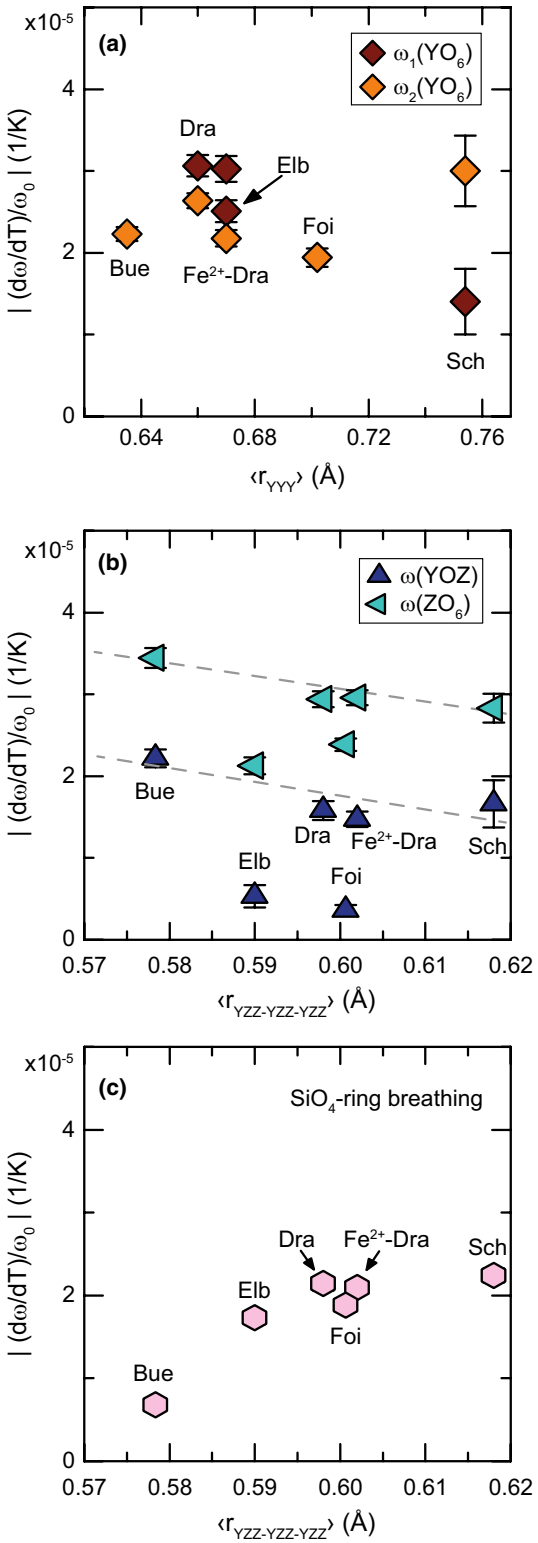

Fig. 5 Phonon thermal expandabilities of **a** the two dominant YO_6-vibrational modes, **b** the two dominant ZO_6 vibrations, and **c** the SiO_4-ring breathing mode at the highest wavenumbers in dependence of tourmaline chemistry expressed by the mean ionic radii of the two octahedral clusters, YZZ–YZZ–YZZ and YYY, respectively. Symbol form and color for the depicted modes correspond to Fig. 3a. *Dashed lines* in **b** are guides to the eye

static thermal expansion by single-crystal XRD for representative iron-containing tourmalines. Changes in the unit-cell parameters were recorded in the temperature range 295–550 K. The thermal expansion was determined from linear fits to the data points. The linear coefficients α_{11} and α_{33}, as well as the volume thermal expansion α_V at reference temperatures $T_0 = 0$ K and $T_{295} = 295$ K are given in Table 2. In comparison with literature data obtained by different experimental techniques [XRD (Donney 1977), strain gauge (Tatli and Pavlovic 1988), interferometry (Krishnan et al. 1979), and dilatometry (Pandey and Schreuer 2012)], the linear expansion coefficients are in reasonably good agreement with the dilatometry as well as strain-gauge and interferometry data. The determined static thermal expansion coefficients at T_0 were then further used to calculate the Grüneisen parameters of selected framework vibrational modes and the dominant ^{V}OH-stretching mode. The values for different tourmalines are summarized in Table 3. On average, the isotropic Grüneisen parameter γ_V of the framework vibrations ranges between 1 and 2. This falls into the expected region for many rock-forming minerals for which γ_V commonly range between 1 and 3 (Chopelas 2000; Hofmeister and Mao 2002; Hunklinger 2009). In general, this implies that the temperature-induced changes in the phonon wavenumbers and the unit-cell volume are of similar order. Interestingly, the γ_V values of the YO_6 as well as of the ZO_6 vibrations are the same for fluor-buergerite and fluor-schorl within the error. This indicates that the valence state of Fe is irrelevant for the ratio between the isotropic dynamic and static response of the lattice to a change in temperature. However, it should be emphasized that the anisotropic Grüneisen parameters for the YO_6 and ZO_6 phonon modes are quite different for fluor-schorl and fluor-buergerite. Furthermore, both the isotropic and anisotropic Grüneisen parameters of the SiO_4 vibrations depend on the oxidation state of Fe. This is most probably related to the fact that the presence of trivalent cations at the Y site disturbs the degree of puckering of the six-membered SiO_4 rings (Mihailova et al. 1996) and consequently enhances the anisotropy in the thermal expansion of tourmalines. Indeed, the thermal-expansion coefficients and consequently the Grüneisen parameters for elbaite also indicate a strong anisotropic elastic response of the crystal to a change in temperature (see Tables 2 and 3). Besides, the dependence of the thermal expandability of the SiO_4-ring breathing mode on $\langle r_{YZZ-YZZ-YZZ} \rangle$ (Fig. 5) indicates that fluor-buergerite and elbaite are in the regime of linear increase, while fluor-schorl is clearly in the saturation regime. This suggests less flexibility in the ring topology in fluor-schorl and therefore less anisotropic response. It is worth noting that, within the uncertainties, the isotropic Grüneisen

Table 2 Linear thermal-expansion coefficients of selected tourmaline species at a reference temperature T_0

Species (#)	α_{11} (10^{-6} K)	α_{33} (10^{-6} K)	α_V (10^{-6} K)	T_0 (K)
Fluor-buergerite (S36)	5.2(4)	10(1)	19.7(9)	0
	5.1(4)	10(1)	19.6(9)	295
Fluor-schorl (S8)	6.4(5)	7(1)	20(1)	0
	6.4(4)	7(1)	20(1)	295
Fe^{2+}-bearing elbaite (S19)	4.2(6)	10.0(7)	18(2)	0
	4.2(6)	9.9(7)	18(2)	295

Digits in parentheses represent the uncertainty (standard deviation) in the last digit of the value

parameters for the SiO_4 modes in elbaite and fluor-schorl are the same compared to fluor-buergerite. This indicates that the isotropic response depends on the average oxidation state of the Y-site cations, which is divalent for both elbaite and fluor-schorl.

The mode Grüneisen parameters for the ^{V}OH-stretching vibration are significantly smaller. However, as the reported average and the mode Grüneisen parameters typically concern the framework vibrations, such differences for vibrational modes of light elements are not surprising.

Oxidation of Fe at elevated temperatures

All previous Raman data stem from experiments in which the tourmaline samples were heated in N_2 atmosphere, which prevents oxidation of incorporated Fe^{2+} and Mn^{2+} and thus simulates thermal expansion behavior in environments with low oxygen fugacity f_{O2}. In contrast, oxidation of Fe^{2+}-bearing tourmalines heated in air is expected at temperatures above 950 K (Pieczka and Kraczka 2004). Thus, Raman spectroscopic measurements at these conditions provide information about the thermal-expansion behavior in environments with high oxygen fugacity. The amount of Fe^{2+} that oxidizes to Fe^{3+} under such conditions depends on temperature and time of annealing (Pieczka and Kraczka 2004; Filip et al. 2012). For charge balancing reasons, the oxidation of Fe^{2+} to Fe^{3+} is accompanied by a decrease in the total OH content according to the following redox reaction (e.g., Pieczka and Kraczka 2004; Filip et al. 2012):

$$^{Y+Z}Fe^{2+} + {}^{V+W}(OH)^{-} + 1/4O_2 \rightarrow {}^{Y+Z}Fe^{3+} + {}^{V+W}O^{2-} + 1/2H_2O. \quad (1)$$

This oxidation process was followed in fluor-schorl (S8) by Raman spectroscopy. As can be seen in Fig. 6, the spectral shape in particular of YO_6 vibrations (200–250 cm^{-1}) and the SiO_4-ring breathing modes (600–715 cm^{-1}) abruptly changes between 1050 and 1150 K, while the intensity of the OH stretching strongly decreases. After subsequent cooling to 303 K, the spectral shape of the framework vibrations resembles that of fluor-buergerite (gray spectrum on top, Fig. 6a) rather than that of fluor-schorl prior to heating and the intensity of the OH-stretching modes recovers only slightly (Fig. 6b).

Table 3 Mode Grüneisen parameter of selected framework vibrational groups and OH-stretching modes of tourmalines

Species (#)	Vibrational groups/mode	γ_{11}	γ_{33}	γ_V
Fluor-buergerite (S36)	YO_6	4.49(2)	2.17(3)	1.11(1)
	ZO_6	8.3(1)	4.0(2)	2.1(5)
	SiO_4-ring	2.21(1)	1.07(1)	0.55(5)
	SiO_4 stretch	3.70(1)	1.79(2)	0.92(1)
	^{V}OH–3^{Y}Fe^{3+Z}Al^{Z}Al	0.733(1)	0.108(2)	0.182(4)
Fluor-schorl (S8)	YO_6	3.45(4)	3.14(1)	1.1(1)
	ZO_6	6.01(2)	5.48(7)	1.95(2)
	SiO_4-ring	2.58(1)	2.35(3)	0.84(2)
	SiO_4 stretch	2.47(1)	2.25(3)	0.80(2)
	^{V}OH–3^{Y}Fe^{2+Z}Al^{Z}Al	0.255(1)	0.232(2)	0.083(3)
Fe^{2+}-bearing elbaite (S19)	YO_6	6.02(3)	2.52(2)	1.37(6)
	ZO_6	5.27(2)	2.21(2)	1.20(6)
	SiO_4-ring	3.89(2)	1.63(2)	0.88(4)
	SiO_4 stretch	3.75(2)	1.57(1)	0.85(4)
	^{V}OH–2^{Y}Li^{Z}Al^{Z}Al–^{Y}Al^{Z}Al^{Z}Al	0.164(1)	0.068(5)	0.037(7)
	^{V}OH–2^{Y}Fe^{2+Z}Al^{Z}Al–^{Y}Al^{Z}Al^{Z}Al	0.140(2)	0.059(5)	0.032(8)

Notes: YO_6 and ZO_6 refer to the dominant vibrations in the spectral region 220–240 cm^{-1} and 370–410 cm^{-1}, SiO_4-ring and SiO_4-stretch to the modes at 639–710 cm^{-1} (611–640 cm^{-1} for S36), and 1010–1065 cm^{-1} (1065–1090 cm^{-1} for S19). Digits in parentheses represent the uncertainty (standard deviation) in the last digit of the value

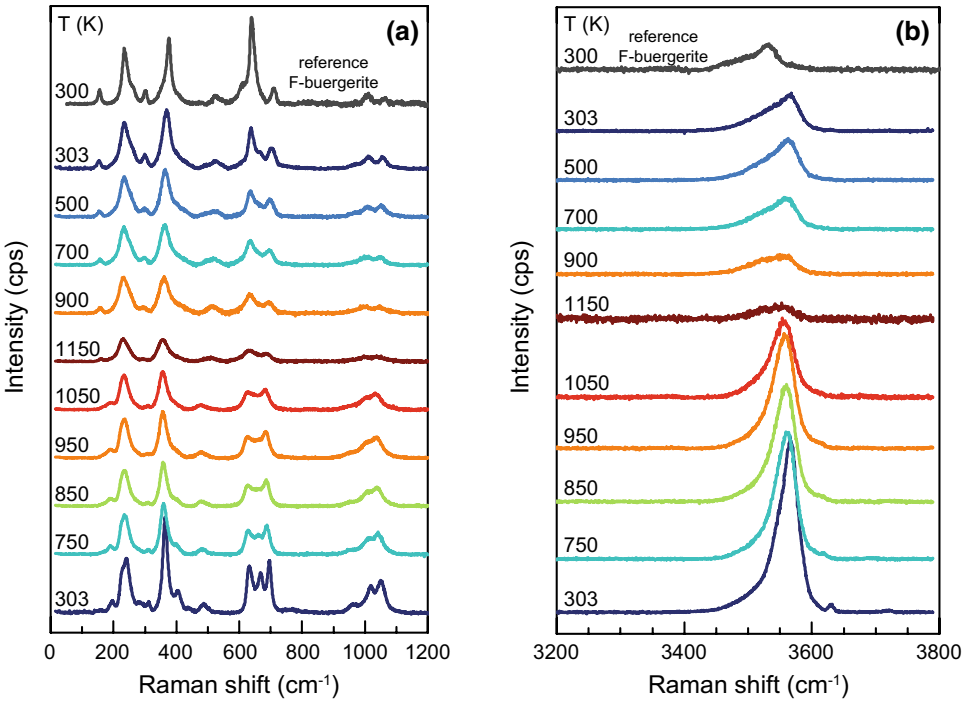

Fig. 6 Temperature-dependent Raman spectra of fluor-schorl (S8) in air atmosphere in the region of the **a** framework vibrations and **b** OH-stretching vibrations. Spectra are vertically offset for clarity. *Numbers* on the *left* indicate the respective temperatures. Note that samples were first heated then cooled, and thus, bottom spectra were taken at the beginning of the temperature run. The *gray spectra* on *top* represent fluor-buergerite (S36) and are plotted for comparison

Figure 7a quantitatively depicts the temperature dependence of the total Raman intensity of the ^{V}OH- and ^{W}OH-stretching modes. Note that all analyzed spectra were normalized to the Bose–Einstein occupation factor of the phonon ground and excited states to eliminate the conventional change in the Raman cross sections with temperature. Thus, all observed changes in the intensities are exclusively related to chemical and/or structural changes of the system. Up to 950 K, there is only a slight decrease in the total intensity, which is most probably related to the beginning of delocalization of H^+ ions via hopping processes. However, the absence of any change in the framework vibrations indicative of Fe^{2+} to Fe^{3+} transformation reveals that the delocalized hydrogen cations are still not ejected from the crystal. This process is strongly enhanced above 950 K, as indicated by the much stronger decrease in the OH-stretching intensity, thus eventually leading to irreversible oxidation of Fe occurring at $T_{ox} = 1050$ K. The characteristic temperature T_{ox} was derived from the temperature dependence of the position of the Raman peak near 312 cm^{-1} (Fig. 7b), generated by vibrations of YO_6–ZO_6 linkages, as well as the wavenumber of highest-energy SiO_4-ring breathing mode near 696 cm^{-1} (Fig. 7d). Our previous study revealed that the wavenumber of the YO_6–ZO_6 vibration, ω_{YOZ}, decreases linearly with the increasing amount of $^{Y}Fe^{3+}$ (Watenphul et al. 2016b). The slope of $\omega_{YOZ}(T)$ abruptly changes at 1050 K (Fig. 7b), leading to a drastic decrease in ω_{YOZ} by 14 cm^{-1} at 1150 K, at which temperature the OH-stretching modes almost vanish. This is due to the oxidation of Fe^{2+} to Fe^{3+} and the simultaneous dehydration of the sample as described by Eq. (1). Such behavior has also been observed for several other minerals including amphiboles (Della Ventura et al. 2017) and mica (Tokiwai and Nakashima 2010). At the same time, the SiO_4-ring breathing mode exhibits a minimum at $T_{ox} = 1050$ K, indicating a structural rearrangement to adopt the silicate ring topology to trivalent cations in the YZZ–YZZ–YZZ clusters (Mihailova et al. 1996; Gasharova et al. 1997), which share oxygen atoms with tetrahedra of the 6-membered rings (see Fig. 1). Furthermore, the FWHM of the SiO_4-ring mode (Fig. 7d) as well as that of the ZO_6 mode near 370 cm^{-1} (Fig. 7c) anomalously increases above T_{ox}, indicating a certain degree of disorder. We attribute this to a thermally induced minor incorporation of Fe^{3+} at the Z site, leading to Fe^{3+}-Al occupancy disorder over the Y and Z sites. After decreasing the temperature to 303 K, the FWHMs of the dominant ZO_6 and the SiO_4-ring mode remain approximately 13 cm^{-1} larger than the corresponding widths of the untreated fluor-schorl and reference fluor-buergerite samples. This unambiguously reveals the preservation of local structural strains associated with the presence of a second type of cation, namely Fe^{3+}, at the Z site.

Upon cooling, the OH-stretching modes slightly regain intensity, indicating a certain extent of recovering of O–H bonds via stabilization of the equilibrium positions of hopping H^+ cations on temperature decrease. The position of the dominant ^{V}OH-stretching mode at 303 K is 3568 cm^{-1} and it matches that of $^{Y}Fe^{2+Z}Al^{Z}Al$-$^{Y}Fe^{2+Z}Al^{Z}Al$-$^{Y}Fe^{2+Z}Al^{Z}Al$ species in

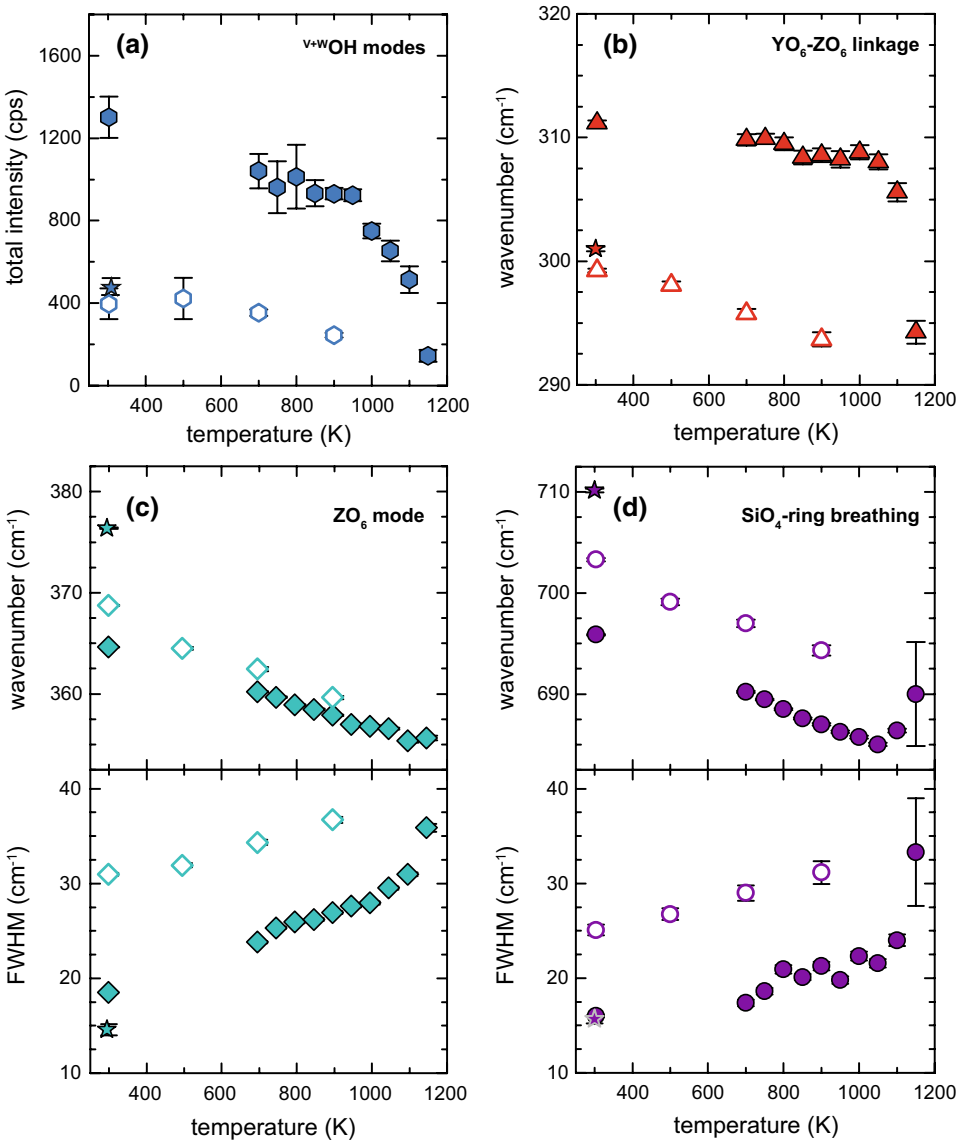

Fig. 7 Temperature dependence of **a** the total integrated intensity of $^{V+W}$OH-stretching modes, **b** the position of the Raman peak related to vibrations of the YO_6–ZO_6 octahedral linkage, **c** the position and FWHM of the dominant ZO_6 vibrational mode, and **d** the position and FWHM of the SiO_4-breathing mode at the highest wavenumber of fluor-schorl (S8) in air atmosphere. Note that *open symbols* refer to data taken upon cooling, while *solid symbols* denote data taken upon heating. Data marked with star symbols originate from fluor-buergerite (S36) and are plotted for comparison

untreated fluor-schorl (Watenphul et al. 2016a), indicating the partial preservation of divalent iron under the heating conditions used. The lower wavenumber OH-stretching peaks are positioned at 3536 and 3500 cm^{-1}. The former is assigned to $^{Y}Fe^{3+Z}Al^{Z}Al$-$^{Y}Fe^{3+Z}Al^{Z}Al$-$^{Y}Fe^{3+Z}Al^{Z}Al$ species, which is the dominant ^{V}OH mode in fluor-buergerite (Watenphul et al. 2016a), while the latter relates to YZZ–YZZ–YZZ species containing both di- and trivalent iron. Interestingly, the total OH-stretching intensity of the heated fluor-schorl sample is the same as that of the reference fluor-buergerite sample (Fig. 7a). However, unambiguous quantitative comparison of the OH loss can hardly be performed solely based on the OH-stretching Raman intensities because of the presence of fluorine combined with O^{2-}/OH^{-} occupancy disorder over the W and V sites (Bosi et al. 2015a, b) as well as the very different Raman cross sections of $^{W}OH^{-}$ and $^{V}OH^{-}$. The wavenumber of the YO_6–ZO_6 linkage mode slightly increases upon cooling due to the unit-cell shrinking (Fig. 7b). At 303 K, ω_{YOZ} is about 12 cm^{-1} lower than for the untreated fluor-schorl sample, i.e., very close to the corresponding peak position of the reference fluor-buergerite sample. This confirms that most of the Y-site divalent iron was oxidized to $^{Y}Fe^{3+}$. Using the trend proposed by Watenphul et al. (2016b), $(^{Y}Fe^{3+}) = 3 \pm 2 - \omega_{YOZ}(7 \pm 1)$, the amount of $^{Y}Fe^{3+}$ in the heated fluor-schorl samples is calculated to 2.1 ± 0.3 apfu. At ambient temperature, the position of the dominant ZO_6 mode recovered to 369 cm^{-1}, which slightly differs from that of the untreated fluor-schorl and is lower than the respective wavenumber for the reference fluor-buergerite. The site occupancy of the latter sample has been determined via combined SC-XRD, Mössbauer spectroscopy and EMPA, revealing that the Z site

is entirely occupied by Al. For tourmaline samples with Al, Fe^{3+}, and Mg dominating at the octahedrally coordinated sites, it has been demonstrated that the Z-site substitution of Fe^{3+} for Al shifts the peak position of the dominant ZO_6 mode toward lower wavenumbers and a second-order polynomial relation between mode wavenumber and the content of the non-aluminum Z-site cations has been proposed (Watenphul et al. 2016b). Thus, an attempt was made to calculate the $^{Z}Fe^{3+}$ content, but the relative error in the obtained value (below 0.5 apfu on average) was too large, hindering the precise quantification of $^{Z}Fe^{3+}$. The presence of trivalent iron at the Z site is, however, robustly confirmed by the increase in the FWHM, as discussed above.

Using the same heating and f_{O2} conditions as those for fluor-schorl (S8), we studied the temperature-dependent changes in the Raman spectra of Fe^{2+}-bearing elbaite (S19) heated in air. In such tourmalines, Fe^{2+} is a minor element, although it is the main extra element compared to the nominal chemistry of elbaite. The presence of iron can be easily judged from the appearance of the ^{V}OH-stretching mode at 3563 cm^{-1} in the Raman spectra at 303 K, which is related to the $2^{Y}Fe^{2+Z}Al^{Z}Al$-$^{Y}Al^{Z}Al^{Z}Al$ octahedral species (Watenphul et al. 2016a). Upon heating, the peak positions of the framework and OH-stretching vibrations as well as the total intensity of the $^{V+W}$OH-stretching modes exhibit only minor changes and peak shifts. Upon cooling, all modes shift back to their initial positions and the total intensity prior and after heating match within uncertainties. It should be underlined that the initial amount of Fe^{2+} in sample S19 was approximately five times less than that in sample S8 (see Table 1), implying that the spectral changes for S19 in case of $Fe^{2+} \rightarrow Fe^{3+}$ exchange would be approximately 20% weaker than those observed for S8. Nevertheless, if Fe oxidation would occur in S19, the expected spectral changes would considerably exceed in absolute magnitude the absolute errors obtained from fitting the spectra. Thus, one can firmly state that the oxidation of Fe incorporated in tourmalines with dominant heterovalent cations at the Y site is strongly suppressed, in contrast to tourmaline species with dominant divalent Y-site cations, like schorl (e.g., Pieczka and Kraczka 2004; Filip et al. 2012; this study) and Fe-bearing oxy-dravite (Bosi et al. 2016). Such behavior might be related to the cationic sizes of the other major elements in the Y and Z site ($^{Y}Fe^{2+}$ = 0.788 Å, $^{Y}Fe^{3+}$ = 0.698 Å, ^{Y}Al = 0.547 Å, ^{Y}Li = 0.751 Å, ^{Y}Mg = 0.723 Å; ionic radii from Bosi and Lucchesi (2007)). The oxidation of iron leads to a decrease in the ionic radius and thus to structural distortions of the YZZ–YZZ–YZZ and YYY configurations proceeding with the adjacent V and W site. Thus, for some tourmaline species, the oxidation might lead to a reduction of local strain and might be favored in those compared to other species.

Conclusions

Our in situ Raman scattering study of Fe-free and Fe^{2+}-rich dravite, Fe^{2+}-bearing elbaite, fluor-schorl, foitite, and fluor-buergerite reveals that the majority of vibrational modes in tourmaline behave regularly with increasing temperature, i.e., the peak position shifts to lower wavenumbers with increasing temperature, while the FWHM increases. Only the lowest energy framework phonon mode and the ^{V}OH-stretching modes related to overcharged YZZ–YZZ–YZZ configurations untypical for the ideal endmember chemistry differ from this behavior.

The dynamic thermal expandability of the ^{V}OH modes shows a distinct dependence on the occupancy of the Y site. In contrast, the phonon thermal expandabilities of the ^{W}OH modes have negligible correlation with the chemistry of the Y site and primarily depend on the occupancy of the X site.

The phonon expandability of the framework vibrational modes points to the reduction of strain due to occupancy disorder of Mg and Al over the Y and Z sites in dravitic tourmalines, while Fe^{2+} at the Y site hinders the suppression of local strain as it shows only a very small tendency to such disorder. Moreover, the expandability of the SiO_4-ring breathing mode with its distinct dependence on the chemistry of the YZZ–YZZ–YZZ octrahedral triplets points to the fact that the chemical composition of the Y and Z sites has a major influence on the topology of the tetrahedral ring.

The linear thermal-expansion coefficients determined by SC-XRD were used together with the Raman spectroscopic data to calculate mode Grüneisen parameters of selected Fe-bearing tourmaline species. It can be seen that on average, the parameters of selected framework vibrational groups fall into the typical range of 1–3 as observed for many rock-forming minerals (Chopelas 2000), while the values of the dominant ^{V}OH-stretching mode are significantly smaller. Our results also demonstrate that tourmalines with smaller mean ionic radius of octahedrally coordinated cations $\langle r_{YZZ-YZZ-YZZ} \rangle$ exhibit stronger anisotropy in the thermal expansion, which is probably related to the effect of the YZZ–YZZ–YZZ triplets on the SiO_4-ring topology. The obtained data can be implemented into thermodynamic models of mineral and rock formation and to gain further information on the macroscopic physical properties.

Additional high-temperature Raman experiments on fluor-schorl and Fe^{2+}-bearing elbaite indicate that at high oxygen fugacity, iron is oxidized only in tourmaline species with homovalent Y-site cations in the ordered chemical

formula. The oxidation process can be easily studied by Raman spectroscopy of both the framework and OH-stretching vibrations. While the reduction of the total intensity of the OH-stretching modes reveals the dehydration accompanying the redox reaction, the phonon wavenumbers, and FWHMs of ZO_6-YO_6 linkage, ZO_6 and SiO_4-ring modes give direct insight into the change from di- to trivalent iron as well as the modification in the ring topology to adapt to the smaller average ionic radius of the octahedrally coordinated cations. Furthermore, thermally induced occupancy disorder of Fe^{3+} over the Y and Z sites was detected in fluor-schorl oxidized to fluor-buergerite. In contrast, iron was not oxidized in Fe^{2+}-bearing elbaite, presumably due to the inability of the crystal structure to compensate the related structural distortion.

Acknowledgements Financial support by the Deutsche Forschungsgemeinschaft DFG (MI 1127/7-1 and SCHL 549/6-1) is gratefully acknowledged. The authors thank P. Stutz for sample preparation, S. Heidrich for conducting electron microprobe analysis, and M. Lensing-Burgdorf for help with the Raman spectroscopic measurements.

References

Bloodaxe ES, Hughes JM, Dyar MD, Grew ES, Guidotti CV (1999) Linking structure and chemistry in the schorl-dravite series. Am Miner 84:922–928

Bosi F, Lucchesi S (2007) Crystal chemical relationships in the tourmaline group: structural constraints on chemical variability. Am Miner 92:1054–1063

Bosi F, Skogby H (2013) Oxy-dravite, $Na(Al_2Mg)(Al_5Mg)(Si_6O_{18})(BO_3)_3(OH)_3O$, a new mineral species of the tourmaline supergroup. Am Miner 98:1442–1448

Bosi F, Andreozzi GB, Federico M, Graziani G, Lucchesi S (2005) Crystal chemistry of the elbaite-schorl series. Am Mineral 90:1784–1792

Bosi F, Balić-Žunić T, Surour AA (2010) Crystal structure analyses of four tourmaline specimens from the Cleopatra's Mines (Egypt) and Jabal Zalm (Saudi Arabia), and the role of Al in the tourmaline group. Am Miner 95:510–518

Bosi F, Skogby H, Agrosì G, Scandale E (2012) Tsilaisite, $NaMn_3Al_6(Si_6O_{18})(BO_3)_3(OH)_3OH$, a new mineral species of the tourmaline supergroup from Grotta d'Oggi, San Pietro in Campo, island of Elba, Italy. Am Miner 97:989–994

Bosi F, Reznitskii L, Skogby H, Hålenius U (2014) Vanadio-oxy-chromium-dravite, $NaV_3(Cr_2Mg_4)(Si_6O_{18})(BO_3)_3(OH)_3O$, a new mineral species of the tourmaline supergroup. Am Miner 99:1155–1162

Bosi F, Andreozzi GB, Hålenius U, Skogby H (2015a) Experimental evidence for partial Fe^{2+} disorder at the Y and Z sites of tourmaline: a combined EMP, SREF, MS, IR and OAS study of schorl. Miner Mag 79:515–528

Bosi F, Skogby H, Lazor P, Reznitskii L (2015b) Atomic arrangements around the O3 site in Al- and Cr-rich oxy-tourmalines: a combined EMP, SREF, FTIR and Raman study. Phys Chem Miner 42:441–453

Bosi F, Skogby H, Hålenius U (2016) Thermally induced cation redistribution in Fe-bearing oxy-dravite and potential geothermometric implications. Contrib Miner Petr 171:47

Bosi F, Skogby H, Ciriotti ME, Gadas P, Novák M, Cempírek J, Všianský D, Filip J (2017) Lucchesiite, $CaFe_3^{2+}Al_6(Si_6O_{18})(BO_3)_3(OH)_3O$, a new mineral species of the tourmaline supergroup. Miner Mag 81:1–14

Chopelas A (2000) Thermal expansivity of mantle relevant magnesium silicates derived from vibrational spectroscopy at high pressure. Am Miner 85:270–278

Della Ventura G, Susta U, Bellatreccia F, Marcelli A, Redhammer GJ, Oberti R (2017) Deprotonation of Fe-dominant amphiboles: single-crystal HT-FTIR spectroscopic studies of synthetic potassic-ferro-richterite. Am Miner 102:117–125

Donney G (1977) Structural meachnism of pyroelectricity in tourmaline. Acta Crystall A33:927–932

Donney G, Barton R Jr (1972) Refinement of the crystal structure of elbaite and the mechanism of tourmaline solid solution. Tscher Miner Petrog 18:273–286

Ertl A, Hughes JM, Prowatke S, Ludwig T, Prasad PSR, Brandstaetter F, Koerner W, Schuster R, Pertlik F, Marschall H (2006) Tetrahedrally coordinated boron in tourmalines from the liddicoatite-elbaite series from Madagascar: structure, chemistry and infrared spectroscopic studies. Am Miner 91:1847–1856

Ertl A, Baksheev IA, Giester G, Lengauer CL, Prokofiev VY, Zorina LD (2016) Bosiite, $NaFe_3^{3+}(Al_4Mg_2)(Si_6O_{18})(BO_3)_3(OH)_3O$, a new ferric member of the tourmaline supergroup from the Darasun gold deposit, Transbaikalia, Russia. Eur J Miner 28:581–591

Filip J, Bosi F, Novák M, Skogby H, Tuček J, Čuda J, Wildner M (2012) Iron redox reactions in the tourmaline structure: high-temperature treatment of Fe^{3+}-rich schorl. Geochim Cosmochim Acta 86:239–256

Gasharova B, Mihailova B, Konstantinov L (1997) Raman spectra of various types of tourmaline. Eur J Miner 9:935–940

Gavrilova ND, Maksimov EG, Novik VK, Drozhdin SN (1989) The low-temperature behavior of the pyroelectic coefficient. Ferroelectrics 100:223–240

Gonzalez-Carreño T, Fernández M, Sanz J (1988) Infrared and electron microprobe analysis of tourmalines. Phys Chem Miner 15:452–460

Hawkins KD, MacKinnon IDR, Schneeberger H (1995) Influence of chemistry on the pyroelectric effect in tourmaline. Am Miner 80:491–501

Hawthorne FC (1996) Structural mechanisms for light-element variations in tourmaline. Can Miner 34:123–132

Hawthorne FC, Lussier AJ, Ball NA, Henry DJ, Shimizu R, Ogasawara Y, Ota T (2016) Maruyamaite, $K(MgAl_2)(Al_5Mg)Si_6O_{18}(BO_3)_3(OH)_3O$, from the ultrahigh-pressure Kokchetav massif, northern Kazakhstan: description and crystal structure. Am Miner 101:355–361

Henry DJ, Dutrow BL (1996) Metamorphic tourmaline and its petrologic applications. In: Grew ES, Anvitz LM (eds) Boron: mineralogy, petrology and geochemistry, Reviews in mineralogy and geochemistry, vol 33. Mineralogical Society of America, Chantilly, pp 503–557

Henry DJ, Novák M, Hawthorne FC, Ertl A, Dutrow BL, Uher P, Pezzotta F (2011) Nomenclature of the tourmaline-supergroup minerals. Am Miner 96:895–913

Hofmeister AM, Chopelas A (1991) Vibrational spectroscopy of end-member silicate garnets. Phys Chem Miner 17:503–526

Hofmeister AM, Mao H-K (2002) Redefinition of the mode Grüneisen parameter for polyatomic substances and thermodynamic implications. P Natl Acad Sci USA 99:559–564

Hunklinger S (2009) Festkörperphysik, 2nd edn. Oldenbourg Wissenschaftsverlag GmbH, p 230

Krishnan RS, Srinivasan R, Devanarayanan S (1979) Thermal expansion of crystals. Pergamon, Oxford, p 162

Kuzmany H (2009) Solid-state spectroscopy—an introduction. Springer, Berlin, p 554

Leissner L, Schlüter J, Horn I, Mihailova B (2015) Exploring the potential of Raman spectroscopy for crystallochemical analyses of complex hydrous silicates: I. Amphiboles. Am Miner 100:2682–2694

Lensing-Burgdorf M, Watenphul A, Schlüter J, Mihailova B (2017) Crystal chemistry of tourmalines from erongo mountains, namibia, studied by raman spectroscopy. Eur J Miner. doi:10.1127/ejm/2017/0029-2607

Mernagh TP (1991) Use of the laser Raman microprobe for discrimination amongst feldspar minerals. J Raman Spectrosc 22:453–457

Mihailova B, Gasharova B, Konstantinov L (1996) Influence on non-tetrahedral cations in Si–O vibrations in complex silicates. J Raman Spectrosc 27:829–833

Momma K, Izumi F (2011) VESTA 3 for three-dimensional visualization of crystal, volumetric and morphology data. J Appl Crystallogr 44:1272–1276

Nishio-Hamane D, Minakawa T, Yamaura J, Oyama T, Ohnishi M, Shimobayashi N (2014) Adachiite, a Si-poor member of the tourmaline supergroup from the Kiura mine, Oita Prefecture, Japan. J Miner Petro Sci 109:74–78

Pandey CS, Schreuer J (2012) Elastic and piezoelectric constants of tourmaline single crystals at non-ambient temperatures determined by resonant ultrasound spectroscopy. J Appl Phys 111:013516

Pieczka A (2000) Modelling of some structural parameters of tourmalines on the basis of their chemical composition. I. Ordered structure model. Eur J Miner 12:589–596

Pieczka A, Kraczka J (2004) Oxidized tourmalines—a combined chemical, XRD and Mössbauer study. Eur J Miner 16:309–321

Porto SPS, Scott JF (1967) Raman spectra of $CaWO_4$, $SrWO_4$, $CaMoO_4$ and $SrMoO_4$. Phys Rev 157:716–717

Schreurs AMM, Xian X, Kroon-Batenburg LMJ (2010) EVAL15: a diffraction data integration method based on ab initio predicted profiles. J Appl Crystallogr 43:70–82

Tatli A, Pavlovic AS (1988) Thermal expansion of tourmaline single crystals from 80 to 300 K. Phys Rev B 38:10072

Tokiwai K, Nakashima S (2010) Integral molar absorptivities of OH in muscovite at 20 to 650 °C by in situ high-temperature IR microspectroscopy. Am Miner 95:1052–1059

Wang A, Jolliff BL, Haskin LA, Kuebler KE, Viskupic KM (2001) Characterization and comparison of structural and compositional features of planetary quadrilateral pyroxenes by Raman spectroscopy. Am Miner 86:90–806

Watenphul A, Burgdorf M, Schlüter J, Horn I, Malcherek T, Mihailova B (2016a) Exploring the potential of Raman spectroscopy for crystallochemical analyses of complex hydrous silicates: II. Tourmalines. Am Miner 101:970–985

Watenphul A, Schlüter J, Bosi F, Skogby H, Malcherek T, Mihailova B (2016b) Influence of the octahedral cationic-site occupancies on the framework vibrations of Li-free tourmalines, with implications for estimating temperature and oxygen fugacity in host rocks. Am Miner 101:2554–2563

Yavuz F, Karakaya N, Yıldırım DK, Karakaya MÇ, Kumral M (2014) A Windows program for calculation and classification of tourmaline-supergroup (IMA-2011). Comput Geosci 63:70–87

Zhao C-C, Liao L-B, Xing J (2014) Correlation between intrinsic dipole moment and pyroelectric coefficients of Fe-Mg tourmaline. Int J Min Met Mater 21:105–112